

CFD-DERIVED PARASITE-DRAG LAW OF AN OCTOCOPTER AIRFRAME WITH ENDURANCE IMPLICATIONS

Kazi Tauhid Mokbul Hussain¹, Mobin Kabir², Irfan Talukder³, Farhan Rahman Atul⁴

^{1,2,3,4}Department of Aeronautical Engineering, Military Institute of Science and Technology, Mirpur Cantonment, Dhaka, Bangladesh

tahiyanhussain7@gmail.com¹, mobin410@gmail.com², accirfan5@gmail.com³, farhanrahmanatul@gmail.com⁴

Abstract- Octocopters are increasingly utilized, but designers lack a straightforward and reliable method for calculating airframe drag, which is critical for accurate power and endurance estimation. This study isolates airframe-induced drag (excluding propellers) using computational simulations of a 7.2-kg octocopter operating at speeds from 1 to 15 m/s. Standard simulation techniques resolve near-wall flow phenomena, and the computational setup is verified for accuracy. Comparative analysis of airflow at 4 and 15 m/s shows that increased drag at higher speeds is mainly due to the expansion of disturbed flow regions, especially at arm–hub and landing-gear junctions, where flow separation and wake formation intensify. The measured drag values closely follow a single airspeed-based formula, allowing straightforward drag prediction within this velocity range. Expressed in terms of electrical power, this law enables determination of optimal cruising speeds for maximum range without further simulations. The results also show that geometric modifications, such as rounding sharp corners at critical junctions and refining landing-gear profiles, can significantly reduce drag.

Keywords: Drone, Aerodynamics, Endurance, Parasite Drag, CFD

1. INTRODUCTION

Multirotor endurance and range are tightly constrained by the high power required to both generate lift and overcome parasite drag in forward flight. Recent studies have combined CFD, wind-tunnel testing, and flight data to quantify multirotor drag and wake development, underscoring how the airframe's bluff components and junctions can dominate the power budget at moderate and higher speeds. In particular, Hammer et al. paired CFD with wind-tunnel measurements to estimate the drag of small Unmanned Aerial Systems (UAS) and demonstrated the value of clean, reproducible drag laws for design-level decisions [1].

At the same time, advanced computer models for multirotors have matured. For example, Ventura Diaz and Yoon developed a method to analyze forward flight aerodynamics, mapping changing airflow patterns during flight and in wind tunnels [2]. Together, these studies demonstrate that accurately predicting drag—separate from rotor effects when necessary—is crucial for reliable estimates of power and endurance [3].

Power–mission analyses reveal that a simple drag–speed relationship is crucial for planning range and endurance, as it directly determines the energy required to cover a distance. Bauersfeld and Scaramuzza's widely used formula links aerodynamic parameters to optimal cruise and time aloft, showing that even small errors in parasite drag can notably skew endurance predictions. Building on this, component-level research reveals the main sources of airframe drag. Götten et al. measured UAV

landing-gear and turret drag using wind tunnel and CFD tests, while other studies documented how bluff-body junctions and appendages create separated regions that thicken the wake with speed [5], [6].

Besides accurate aerodynamic modeling, best practices in CFD have become clear, particularly regarding model choices and the required numerical rigor for publication. The $k-\omega$ SST model remains a common standard for attached or separated external flows when near-wall resolution is present; NASA's Turbulence Modeling Resource offers standardized versions. At the same time, validation guidance now spells out expectations for grid refinement and uncertainty reporting, which are now common even in application-focused external-aero studies [7].

Despite these advances, few studies systematically isolate and characterize the airframe-only drag of octocopter-class vehicles across multiple forward speeds. Specifically, there is a lack of work that (i) yields a portable, single-parameter drag law for design and operation; (ii) is supported by mesh and solver verification at a reference condition; and (iii) connects directly to power mapping and operational set-points without further simulation. Much of the literature focuses on rotor–body interaction or reports drag for quadrotor archetypes, leaving a gap for octocopters, which differ in planform, arm–hub junctions, and landing-gear layouts [2],[8]. This context motivates the present study.

To address this gap, the present study conducts a CFD-based investigation of airframe drag for a 7.2-kg

octocopter. The methodology includes: (i) defining a reproducible setup with near-body meshing and $k-\omega$ SST turbulence closure; (ii) verification at a reference speed; (iii) reporting flow evidence at 4 m/s and 15 m/s to identify regions of separation and wake thickening; and (iv) consolidating force extractions at four speeds into a single quadratic drag–speed relation for direct application in power budgeting and range-optimal cruise selection without further CFD analysis. The approach follows established community guidelines for turbulence modeling and verification. The discussion connects observed flow structures to design strategies identified in prior research, emphasizing opportunities for effective drag reduction [9], [10].

To further clarify the scope and applicability of these results, the findings are positioned alongside complementary multirotor and UAV literature, including CFD analyses near obstacles [11] and studies of overlapping-rotor configurations [12]. Although the primary focus is airframe drag with propellers inactive, these related studies offer important context for integrating the present airframe law into broader mission models.

2. THEORY

The octocopter airframe is considered in uniform, low-speed external flow (1–15 m/s), modeled as incompressible and viscous. The drag campaign isolates airframe parasitic drag; rotors are excluded from the main cases. The fitted drag parameter is estimated in Section 3 and used in Section 4 to interpret fields, quantify penalties, and select a cruise set-point.

2.1 Airframe drag model and fitting

To compress the CFD force data into a portable relation, a quadratic drag–speed is adopted:

$$D(V) = a \cdot V^2 \quad (1)$$

where D is the streamwise drag at airspeed V and $a > 0$ aggregates density and an effective drag coefficient. We enforce the physical condition $D(0) = 0$ by regressing D on V^2 with zero intercept.

2.2 Parasitic Electrical Power

The mechanical work rate against drag is $D \cdot V$. Mapping to the electrical side with η gives the parasitic increment using the fitted drag parameter from (1):

$$P_{\text{par}}(V) = k \cdot V^3 \quad (2)$$

where $k = a / \eta$ and η is the system's electrical efficiency. This value represents the additional electrical power required due to airframe drag during forward flight or when maintaining position against a headwind.

2.3 Cruise Power and Optimal Speed

For the speed range considered, non-parasitic terms vary weakly with V , so a practical total-power model is

$$P(V) = P_0 + k \cdot V^3 \quad (3)$$

with P_0 taken from bench propulsion data and k from the CFD-inferred via equation (2). Minimizing energy per distance yields a closed-form range-optimal cruise

speed:

$$V^* = \left(\frac{P_0}{2k} \right)^{\frac{1}{3}} \quad (4)$$

which links the CFD-inferred drag directly to an operational set-point.

3. METHODOLOGY

This section documents the geometry prepared for CFD, including the external-flow domain and boundary conditions, meshing and wall treatment, turbulence modeling and numerical methods, the convergence and verification procedure, and the force extraction and fitting used to obtain the airframe drag law introduced in section 2.

3.1 Geometry and Reference Quantities

The CFD model is the manufactured octocopter used here in fig. 1: an octagonal hub with 440 mm hub-to-motor arms, carbon-fiber top and bottom plates, and four carbon-fiber landing-gear tubes. External fasteners and cable runs are omitted to avoid small-feature artefacts that do not materially change bluff-body drag at the tested speeds. The body frame is fixed at the hub center, with x forward and z downward; the freestream aligns with the $+x$ direction. Air density is assumed to be constant over the sweep.

3.2 Domain and Boundary Conditions

The airframe is placed in a rectangular external-flow enclosure sized to suppress blockage and recirculation as shown in fig. 2. The inlet lies at least three characteristic diameters upstream of the foremost point; the outlet is at least ten diameters downstream; lateral and top boundaries are at least five diameters from the geometry envelope. Boundary conditions follow table 1: a uniform inlet speed V for each case, pressure outlet set to ambient static pressure, symmetry on the side and top planes.

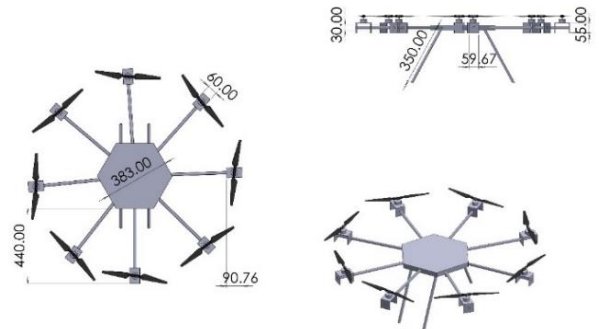


Fig.1: Octocopter airframe used for CFD drag studies

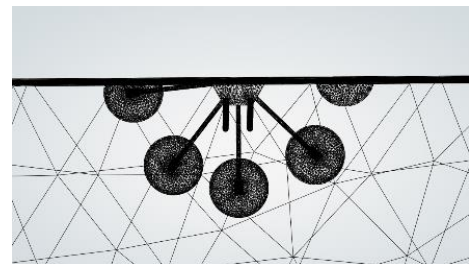


Fig.2: Computational domain and near-body mesh

Table 1: CFD setup for airframe drag cases

Parameter	Setting
Flow model	3D incompressible, steady RANS, pressure-based solver
Turbulence	k- ω SST
Spatial discretization	Second order upwind
Computational domain	Rectangular enclosure ($10 \times 2 \times 2$ m)
Inlet	Velocity inlet
Outlet	Pressure outlet
Mesh Type	Unstructured tetrahedral
Near-body mesh	Element size 5 mm
Far-field mesh	Element size 300-600 mm
Domain extents	$\geq 3D$ upstream, $\geq 10D$ downstream
Wall Treatment	No-slip, $Y^+ : 1$
Rotors modeled in runs	No (airframe only)
Initial Conditions	Pressure 101325 Pa, Temperature = 298 K
Convergence	Residuals $\leq 1 \times 10^{-4}$

3.3 Mesh generation and near-wall resolution

The computational domain is discretized into a mesh of three-dimensional elements, with increased resolution near the airframe surface. Near-surface elements are approximately 5 mm in size and expand with distance from the geometry, as specified in table 1. Twelve prism layers are applied adjacent to the surfaces, each increasing in thickness to resolve wall effects and ensure precise force measurement at the boundary. Drag forces are calculated exclusively on the airframe surfaces.

3.4 Convergence, monitoring and solution

Each simulation begins with a mixed initial air state and continues until it meets two requirements: the checks on simulated residuals must drop below 1×10^{-4} for key flow equations, and the calculated drag on the drone must remain steady within 0.1% over the last 500 calculation cycles. After finishing one speed, the results can help start the next simulation at a new speed, using the same quality checks. For every case, we save the progress records, drag history, and summary files generated by the simulation program.

3.5 Verification and sensitivities

To verify numerical resolution of the reported forces, the solution at a representative speed was repeated on systematically refined meshes based on the baseline configuration in table 1, maintaining the same surface sizing strategy, prism-layer count and growth, and first-cell height set for $y^+ = 1$ at the highest speed.

Physics and numerics were held constant across all grids, employing incompressible steady RANS, k- ω SST, and second-order spatial discretization. Throughout the refinement sequence, integrated drag exhibited the expected monotonic trend, and the difference between the two finest mesh levels was small relative to the variation in drag across the speed sweep. The finest mesh was therefore selected for simulations at $V = 1, 4, 7$, and 15 m/s.

3.6 Drag-law Regression

The CFD force extractions are consolidated into a portable law by regressing D on V^2 with the intercept fixed at zero, thereby enforcing $D(0) = 0$. The fitted slope a , its coefficient of determination (R^2), and a 95% confidence interval are reported. The fitted value of a is subsequently used in Section 4 to generate the drag-speed curve and interpret the flow fields.

3.7 Propeller Model and MRF Setup

To ensure the propulsion mapping used later in the paper is physically reasonable, an isolated propeller is modeled with a cylindrical Multiple-Reference-Frame rotating zone, shown in figs. 3-5. Surface pressure and velocity distributions on the upper side at a representative advance condition are shown in fig. 6(a-b) as a qualitative check. These runs are strictly contextual; no rotor modeling is included in the airframe drag cases.

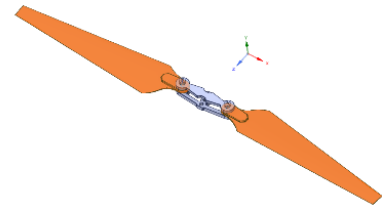


Fig.3: Propeller used for the MRF model

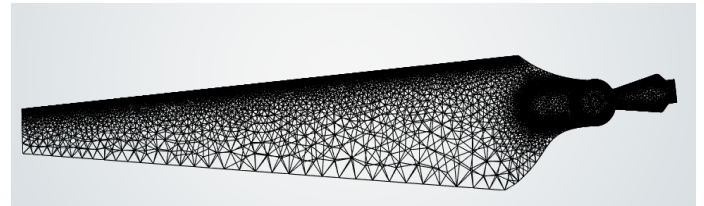


Fig.4: Blade-hub surface mesh for the MRF rotor with near-blade refinement (growth rate 1.2).

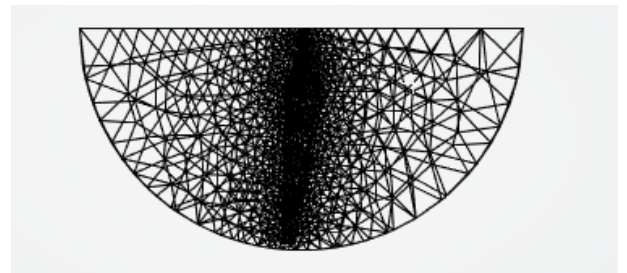


Fig.5: MRF rotating zone around the propeller, rotating inner and stationary outer regions with local mesh

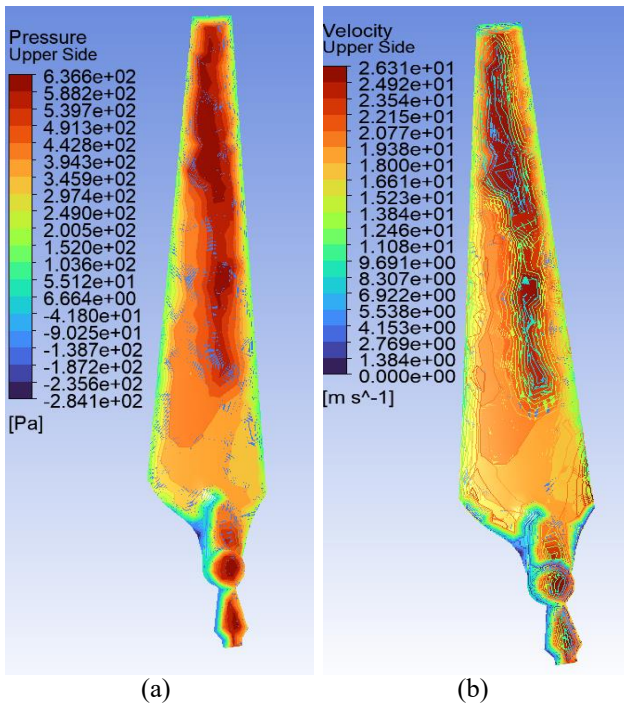


Fig.6: Propeller MRF validation on the upper surface at $V = 4$ m/s and $n = 1000$ rpm (a) surface pressure (Pa) and (b) surface velocity (m/s)

4. RESULT AND DISCUSSION

4.1 Flow Fields at Low and High Wind

Mid-plane contours at freestream velocities of 4 m/s and 15 m/s are presented in figs. 7–10. At 4 m/s, pressure extremes are concentrated at the leading edges of the arms and landing gear, with shear layers remaining attached and rapid wake recovery observed. At 15 m/s, expanded suction regions form at arm–hub and landing-gear junctions, shear layers thicken and merge, and the wake extends further downstream with localized recirculation behind bluff components. This transition indicates a shift from predominantly attached flow with minor separation to a regime dominated by flow separation, where pressure drag becomes the primary contributor to drag. These findings elucidate the mechanisms responsible for increased drag and identify specific geometric regions that are potential targets for improvement.

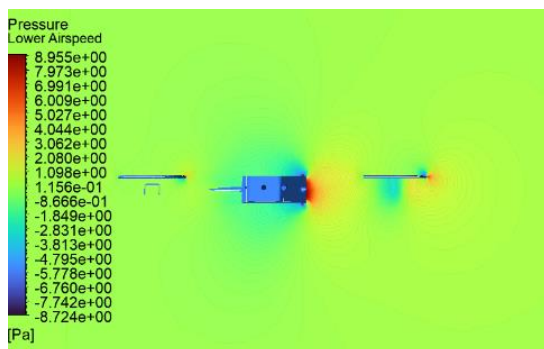


Fig.7: Pressure contour (Pa) at $V = 4$ m/s

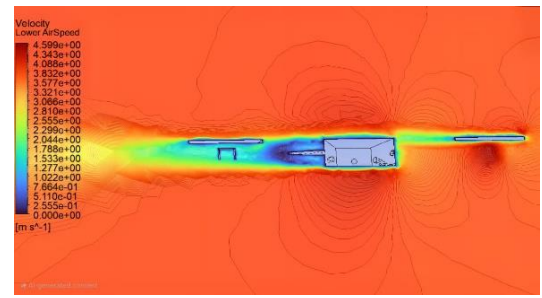


Fig.8: Velocity magnitude (m/s) at $V = 4$ m/s

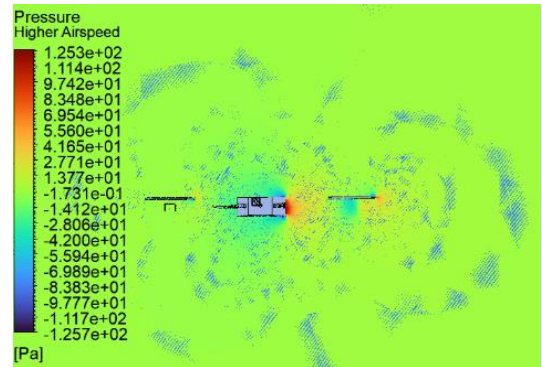


Fig.9: Pressure contour (Pa) at $V = 15$ m/s

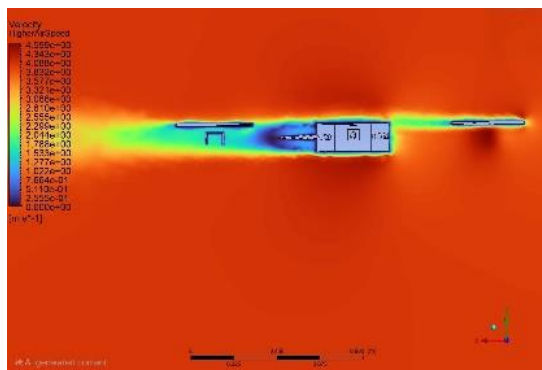


Fig.10: Velocity magnitude (m/s) at $V = 15$ m/s

4.2 Drag–Speed Curve from CFD

The CFD force extractions at headwind $V = \{1, 4, 7, 15\}$ m/s (airframe only, propellers off) produce the streamwise drag D , listed in table 2. A least-squares fit constrained through the origin yields $D(V) = 0.0461V^2$, $R^2 = 0.9999$, shown in fig. 11.

Table 2 also presents the mechanical work rate and corresponding electrical power penalty, calculated using the specified efficiency. The increase at higher speeds is substantial; at 15 m/s, the electrical penalty is significantly greater than at 7 m/s, despite the relatively small increase in speed. The fitted parameter from fig. 11 defines the power–speed relationship up to the measured baseline, enabling direct selection of cruise set-points without additional computational fluid dynamics simulations.

Table 2: CFD drag and derived wind-hold power

V (m/s)	Drag, D (N)	DV (W)	D V/η [†] (W)
1	0.0490919	0.049	0.058
4	0.751892	3.008	3.538
7	2.27657	15.936	18.748
15	10.3681	155.522	182.966

[†]Overall shaft-to-electric efficiency 0.85

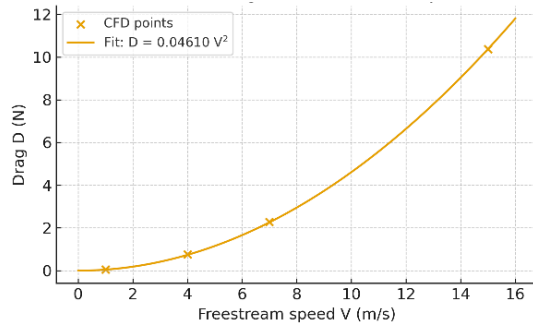


Fig.11: Airframe drag vs freestream speed; quadratic fit

5. CONCLUSION

This study quantified airframe-only drag for a 7.2-kg octocopter across velocities from 1 to 15 m/s, consolidating the force data into a single quadratic drag–speed relationship with high correlation. Refinement at a reference speed confirmed monotonic drag behavior, while analysis of endpoint flow fields attributed increased drag to the emergence of separation-dominated wakes at higher speeds. The derived law enables direct application to power budgeting and cruise speed selection when combined with measured baseline power and efficiency. Flow field evidence identifies arm–hub and landing-gear junctions, as well as abrupt cross-section changes, as primary sources of drag; thus, filleting and frontal-area reductions are recommended for maximum benefit. Future research will integrate rotor effects and experimentally validate fairing strategies in flight tests.

6. REFERENCES

- [1] T. Hammer, J. Quitter, J. Mayntz, and J.-M. Bauschat, “Free fall drag estimation of small-scale multirotor unmanned aircraft systems using computational fluid dynamics and wind tunnel experiments,” *CEAS Aeronautical Journal*, vol. 15, no. 2, pp. 269–282, Apr. 2024, doi: 10.1007/s13272-023-00702-w.
- [2] P. Ventura Diaz and S. Yoon, “High-fidelity computational aerodynamics of multi-rotor unmanned aerial vehicles,” in *AIAA SciTech 2018 Forum (AIAA Aerospace Sciences Meeting)*, Kissimmee, FL, USA, Jan. 2018, Paper 2018-1266, doi: 10.2514/6.2018-1266.
- [3] C. C. Wolf, D. Schanz, C. Schwarz, et al., “Volumetric wake investigation of a free-flying quadcopter using Shake-The-Box Lagrangian particle tracking,” *Experiments in Fluids*, vol. 65, Art. no. 152, 2024, doi: 10.1007/s00348-024-03880-3.

10.1007/s00348-024-03880-3.

- [4] L. Bauersfeld and D. Scaramuzza, “Range, endurance, and optimal speed estimates for multicopters,” arXiv:2109.04741, v3, Apr. 2024. doi: 10.48550/arXiv.2109.04741.
- [5] F. Götten, M. Havermann, C. Braun, M. Marino, and C. Bil, “Wind-tunnel and CFD investigations of UAV landing gears and turrets—Improvements in empirical drag estimation,” *Aerospace Science and Technology*, vol. 107, Art. no. 106306, Dec. 2020, doi: 10.1016/j.ast.2020.106306.
- [6] G. Throneberry, A. Takeshita, C. M. Hocut, F. Shu, and A. Abdelkefi, “Wake Propagation and Characteristics of a Multi-Rotor Unmanned Vehicle in Forward Flight,” *Drones*, vol. 6, no. 5, p. 130, 2022, doi: 10.3390/drones6050130
- [7] NASA Langley Research Center, “Turbulence Modeling Resource,” last updated Jun. 3, 2025. Accessed: Sep. 29, 2025. [Online]. Available: <https://turbmodels.larc.nasa.gov>.
- [8] M. Ghirardelli, S. T. Kral, N. C. Müller, R. Hann, E. Cheynet, and J. Reuder, “Flow Structure around a Multicopter Drone: A Computational Fluid Dynamics Analysis for Sensor Placement Considerations,” *Drones*, vol. 7, no. 7, Art. no. 467, 2023, doi: 10.3390/drones7070467.
- [9] C. Paz, E. Suárez, C. Gil, and C. Baker, “CFD analysis of the aerodynamic effects on the stability of the flight of a quadcopter UAV in the proximity of walls and ground,” *Journal of Wind Engineering and Industrial Aerodynamics*, vol. 206, Art. no. 104378, 2020, doi: 10.1016/j.jweia.2020.104378.
- [10] Y. Lei, J. Wang, and Y. Li, “The Aerodynamic Performance of a Novel Overlapping Octocopter Considering Horizontal Wind,” *Aerospace*, vol. 10, no. 10, Art. no. 902, Oct. 2023, doi: 10.3390/aerospace10100902.
- [11] F. Pätzold, A. Bauknecht, A. Schlerf, D. Sotomayor Zakharov, L. Bretschneider, and A. Lampert, “Flight Experiments and Numerical Simulations for Investigating Multicopter Flow Field and Structure Deformation,” *Atmosphere*, vol. 14, no. 9, Art. no. 1336, 2023, doi: 10.3390/atmos14091336.
- [12] M. Kwon and Y. Eun, “Quadrotor dynamics in a wind field: Equilibria analysis and energy dissipation,” *International Journal of Control, Automation and Systems*, vol. 22, no. 11, pp. 3275–3284, Nov. 2024, doi: 10.1007/s12555-024-0048-4.

7. NOMENCLATURE

Symbol	Meaning	Unit
a	Drag law parameter	Ns^2/m^2
k	Power mapping parameter	Ns^2/m^2
V	Freestream Velocity	m/s
P _{par}	Parasitic electrical power	W
P ₀	Baseline electrical power	W
D	Drag	N
V*	Range-optimal cruise speed	m/s
y ⁺	Wall-unit distance	—